Supplemental Methods 1. Study Population

AI-Hub dataset consisted of 30,000 echocardiographic examinations retrospectively collected from five tertiary hospitals, including Chungnam National University Hospital, Hanyang University Hospital, Seoul National University Bundang Hospital, Severance Hospital, and Soonchunhyang University Seoul Hospital, over the period from 2012 to 2021. It encompasses a wide range of cardiovascular disease categories, from normal cases to ischemic heart disease, cardiomyopathy, pulmonary hypertension and embolism, pericardial disease, valvular heart disease, cardiac mass, and congenital heart disease. Data collection was based on diagnostic codes and echocardiographic reports to achieve targeted sample sizes; however, consecutive patient sampling was not enforced.

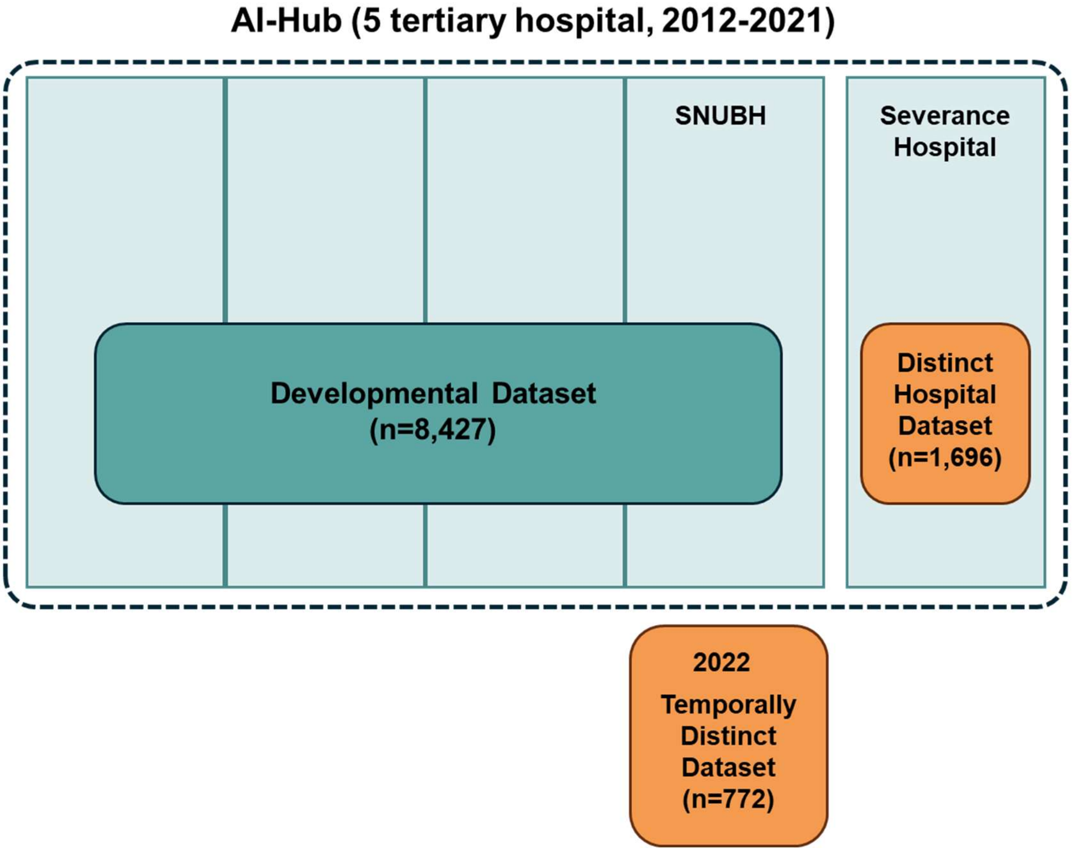
AI-Hub (5 tertiary hospital, 2012-2021)
SNUBH
Severance Hospital
Developmental Dataset (n=8,427)
Distinct Hospital Dataset (n=1,696)
2022
Temporally Distinct Dataset (n=772)

The AI-based frameworks introduced here were all developed using data extracted from the

AI-Hub dataset. Specifically, the DL-based AS continuum assessment algorithm was developed using the **Developmental Dataset (DDS)** sourced from the AI-Hub. During the assembly of DDS, data from Severance Hospital were deliberately excluded and used for external validation. We initially screened transthoracic echocardiography (TTE) data from 4,563 patients diagnosed with aortic stenosis (AS). After excluding those who had undergone aortic valve (AV) replacement or open-heart surgery, those with moderate or greater AV regurgitation, or cases where the severity of AS could not be determined, 4,018 patients with AS have remained. To ensure the model's accuracy, 628 cases exhibiting discordant findings among aortic valve (AV) peak velocity (V_{max}), mean pressure gradient (mPG), and aortic valve area (AVA) regarding the severity of AS were excluded. These cases were later used separately for validating the model. Among the 3,390 patients diagnosed for AS included in the model development, 2,500, 516, and 374 were categorized into mild, moderate, and severe AS, respectively. Additionally, for the purpose of model training, TTE examinations were extracted for 3,290 individuals demonstrating normal AV morphology and function and 1,747 individuals exhibiting signs of AV sclerosis—characterized by degenerative changes in the AV but not meeting the diagnostic criteria for AS. Consequently, TTE data from a total of 8,427 individuals were compiled into the DDS. These data were split in an 8:1:1 ratio for training, validation, and internal testing purposes.

The **Distinct Hospital Dataset (DHDS)** was compiled by reviewing data from Severance Hospital that were not included in the DDS sourced from the AI-Hub dataset. A total of 719 patients with AS were reviewed, none of whom had undergone AV replacement or open-heart surgery. After excluding 60 patients with moderate or greater AV regurgitation, the dataset included 659 patients with AS (209 mild, 251 moderate, and 199 severe). Adding 1,037 normal patients, the DHDS totaled 1,696 patients. Since Severance Hospital does not commonly use the diagnosis of AV sclerosis, a separate AV sclerosis category was not included.

For the **Temporally Distinct Dataset (TDDS)**, we screened TTE data conducted in 2022 at Seoul National University Bundang Hospital, identifying 520 consecutive patients with AS. After excluding cases with a documented history of AV replacement or open-heart surgery, those with moderate or greater AV regurgitation, or cases where the severity of AS could not be determined, a total of 443 patients with AS remained (313 mild, 75 moderate, and 55 severe). Additionally, 55 individuals with normal AV and 274 with AV sclerosis, identified during the same period, were included, resulting in a total of 772 cases included for this dataset.

Supplemental Methods 2. View Classification Networks Update

To enhance our echocardiographic view classification algorithm, we expanded our datasets and refined the classification algorithm to include new views. Building upon our previous work, the dataset was broadened to encompass more granular classifications and additional views.[1] Specifically, we differentiated the parasternal long-axis (PLAX) zoomed view into four distinct categories: PLAX zoomed aortic valve (AV) (779 videos), PLAX zoomed mitral valve (MV) (279 videos), PLAX zoomed both AV and MV (1,357 videos), and PLAX zoomed aorta (502 videos). Additionally, we incorporated 663 CW Doppler AV images obtained from the right parasternal view. These enhancements are crucial for accurately measuring AV stenosis (AS) parameters, such as left ventricular outflow tract (LVOT) diameter, AV maximum velocity (V_{max}), mean pressure gradient (mPG), and AV area (AVA), which are critical for evaluating the severity of AS. The new data points were annotated using a Developmental Dataset (DDS), and the view classification network was subsequently retrained with this enriched dataset, employing the methodology previously detailed in our research.[1]

The tables clearly show the exact number of views used in training for each category, offering a comprehensive count for the latest version of our view classification algorithm.

Target Views for Current Version of View Classification Algorithm.

Echo Mode	Echocardiographic View	Number of Views
B-mode	Parasternal long-axis left ventricle	7,202
	Parasternal long-axis zoomed AV	779
	Parasternal long-axis zoomed MV	279
	Parasternal long-axis zoomed AV & MV	1,357
	Parasternal long-axis zoomed aorta	502
	Parasternal short-axis, level of great vessels	2,959

	Parasternal short-axis, level of mitral valve	5,967
	Parasternal short-axis, level of papillary muscle	6,635
	Parasternal short axis, level of apex	7,143
	Apical four-chamber	4,647
	Apical four-chamber zoomed left ventricle	5,977
	Apical four-chamber right ventricular-focused	2,767
	Apical five-chamber	1,325
	Apical two-chamber	3,035
	Apical two-chamber zoomed left ventricle	5,708
	Apical three-chamber	2,535
	Apical three-chamber zoomed left ventricle	5,500
	Subcostal four-chamber	3,233
	Subcostal long axis IVC	2,717
M-mode	M-mode through left ventricle	3,879
	M-mode through aorta and left atrium	2,788
	M-mode tricuspid annular plane systolic excursion	708
Spectral and tissue Doppler	PW Doppler mitral valve	6,816
	TDI mitral valve lateral annulus	6,388
	TDI mitral valve septal annulus	705
	CW Doppler mitral stenosis	1,811
	CW Doppler mitral regurgitation	1,473
	PW Doppler left ventricular outflow tract	4,262
	CW Doppler aortic valve	3,864
	CW Doppler aortic valve in parasternal	663
	CW Doppler aortic regurgitation	1,094
	CW Doppler tricuspid regurgitation	8,910
	PW Doppler right ventricular outflow tract	2,935
	CW Doppler pulmonic valve	643
	CW Doppler pulmonic regurgitation	748
	Pulmonary vein flow	1,701
	Total	119,655

AV, aortic valve; CW, continuous wave; IVC, inferior vena cava; MV, mitral valve; PW, pulse wave; TDI, tissue Doppler imaging

Supplemental Methods 3. DL-based AS Continuum Assessment Algorithm

Given an input video, we used the r2plus1d architecture as a backbone.[2] Importantly, we modified the backbone network to avoid temporal down-sampling by maintaining a stride of 1 along the temporal axis. In addition to r2plus1d, we evaluated alternative backbone architectures, specifically r3d and mc3, to ensure that our model's performance was not dependent on a single feature extractor. The performance comparison among these backbones, detailed in the following Table, demonstrates consistent accuracy across configurations, with r2plus1d achieving competitive results.

Comparisons analysis of backbone architecture

	mc318	r3d18	r2p1d18
ITDS			
any AS	0.956	0.959	0.952
significant AS	0.955	0.968	0.951
severe AS	0.971	0.974	0.972
DHDS			
any AS	0.996	0.997	0.997
significant AS	0.847	0.805	0.832
severe AS	0.897	0.890	0.899
TDDS			
any AS	0.902	0.898	0.899
significant AS	0.947	0.942	0.946
severe AS	0.977	0.979	0.982

From this feature $\boldsymbol{z}$, we employ four decoders, three of which are designed to predict continuous variables such as AV V$_{\text{max}}$, mPG, and AVA. Each auxiliary decoder is constructed to predict these continuous variables through regression. Each auxiliary decoder consists of two hidden layers with 512 units each, batch normalization and ReLU activation, followed by an output layer with a single unit and a Softplus activation function to ensure positive output values.

We then implemented a fusion module, termed the Adaptive Feature Fusion Module (AFFM), that generates a score for each continuous feature and then fuses them into one feature by a weighted sum of all features according to their scores. For features $z_{v_{max}}, z_{mPG}, z_{AVA}$ from the three auxiliary decoders before the output layer with a single unit, the fusion module computes a weight $w_{v_{max}}, w_{mPG}, w_{AVA}$ for each feature $z_{v_{max}}, z_{mPG}, z_{AVA}$ using a fully connected layer followed by batch normalization, ReLU activation, and a final fully connected layer with sigmoid activation. The fused feature z^{fused} is then computed as a weighted sum of the features: $z_{fused} = w_{v_{max}} z_{v_{max}} + w_{mPG} z_{mPG} + w_{AVA} z_{AVA}$

The fused feature z^{fused} is then concatenated with the original feature z from the r2plus1d backbone, resulting in the final feature z_{final}: $[z; z_{fused}]$. The final classifier classifier processes this concatenated feature z^{final} by linear function followed by a sigmoid function: $\widehat{y_{final}} = sigmoid(Wz_{final} + b)$.

Input videos were resized to 224 x 224, and normalization was applied to a [0, 1] range for both training and inference. During training, if the number of frames exceeded the specified clip length (16 frames), a random start index was selected, motivated by the approach in Holste G et al.[3] If the number of frames was fewer, indices were evenly spaced to fit the clip length. For inference, the videos were divided into four intervals and stacked. If the total frames in the video are sufficient, the video is divided into multiple intervals with evenly spaced start indices. Each interval begins at a calculated start index, ensuring consistent spacing across the video's duration. A sequence of frames matching the clip length is then sampled from each start index, providing a balanced temporal coverage. If the frames were insufficient for multiple intervals but exceeded the clip length, the video was sampled, and the clip was replicated to match the intervals. If the frames were fewer than the clip length, indices were evenly spaced, and the clip was duplicated to match the intervals. The stacked inputs from the inference phase are averaged to enhance the model's generalization capabilities. The final DL index for AS continuum (DLi-ASc) was rescaled to 0-100 by multiplying the model output after the sigmoid function by 100.

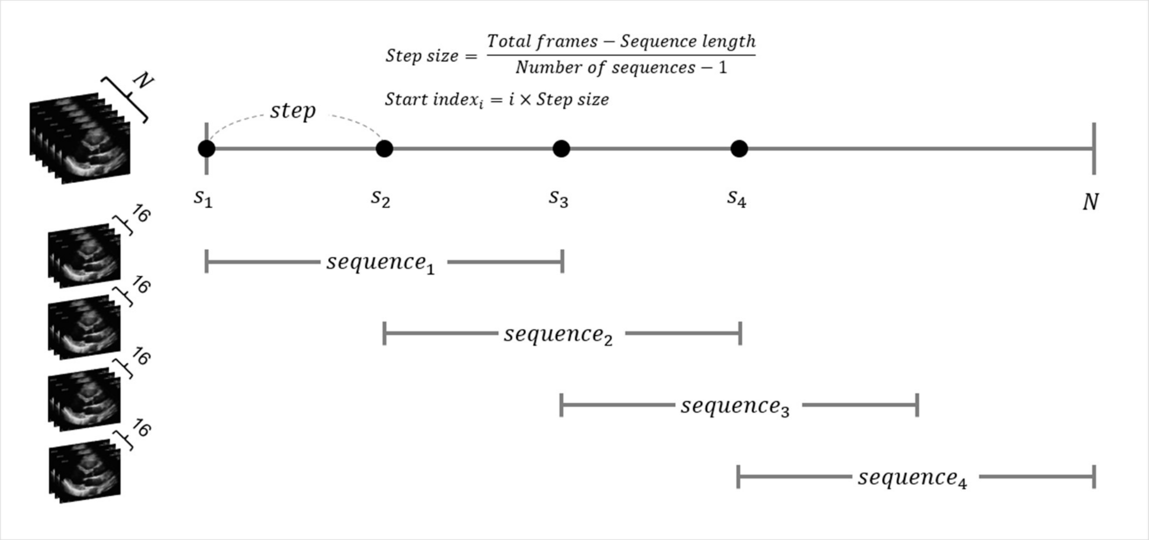
$Step\ size = \frac{Total\ frames - Sequence\ length}{Number\ of\ sequences - 1}$
$Start\ index_i = i \times Step\ size$
step
N
s_1
s_2
s_3
s_4
N
16
16
16
16
$sequence_1$
$sequence_2$
$sequence_3$
$sequence_4$

During training, a class sampler was used to balance the sampling of normal and AS classes by assigning higher weights to the less frequent class. The Adam optimizer was used with a learning rate of 0.0001 and a batch size of 28. No learning rate scheduler was utilized. Early stopping was implemented with a tolerance of 300 epochs, monitoring the validation loss as the metric. Additionally, in cases where ground-truth data for clinical variables such as AV V_{max}, mPG, and AVA were missing, the loss calculation for those instances resulted in a NaN value, which was excluded from the loss computation, ensuring that these instances did not affect model weight updates.

Deep Learning Architecture for DLi-ASc

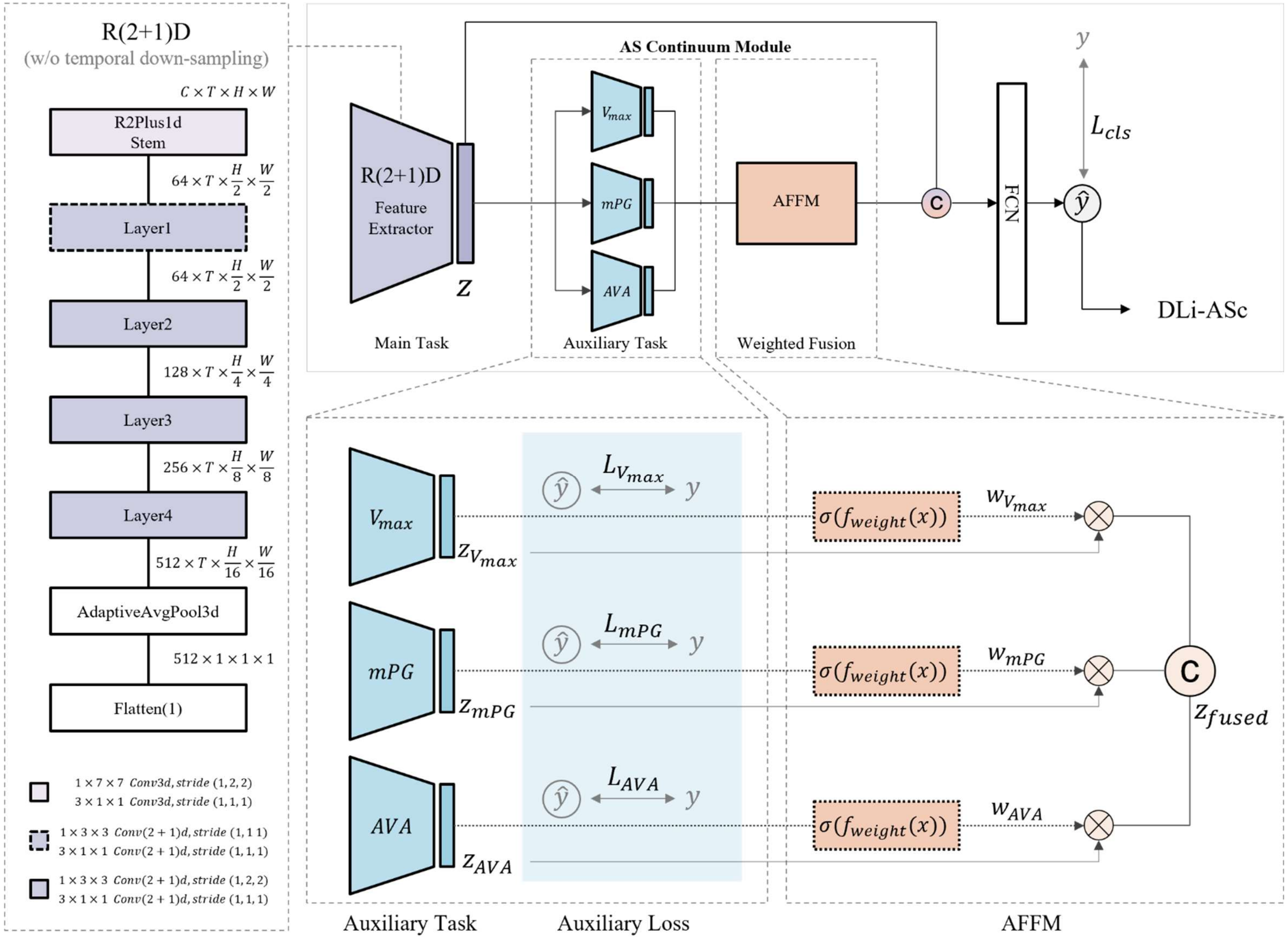
R(2+1)D
(w/o temporal down-sampling)
$C \times T \times H \times W$
R2Plus1d Stem
$64 \times T \times \frac{H}{2} \times \frac{W}{2}$
Layer1
$64 \times T \times \frac{H}{2} \times \frac{W}{2}$
Layer2
$128 \times T \times \frac{H}{4} \times \frac{W}{4}$
Layer3
$256 \times T \times \frac{H}{8} \times \frac{W}{8}$
Layer4
$512 \times T \times \frac{H}{16} \times \frac{W}{16}$
AdaptiveAvgPool3d
$512 \times 1 \times 1 \times 1$
Flatten(1)
$1 \times 7 \times 7$ Conv3d, stride (1, 2, 2)
$3 \times 1 \times 1$ Conv3d, stride (1, 1, 1)
$1 \times 3 \times 3$ Conv(2 + 1)d, stride (1, 1 1)
$3 \times 1 \times 1$ Conv(2 + 1)d, stride (1, 1, 1)
$1 \times 3 \times 3$ Conv(2 + 1)d, stride (1, 2, 2)
$3 \times 1 \times 1$ Conv(2 + 1)d, stride (1, 1, 1)
AS Continuum Module
R(2+1)D Feature Extractor
Z
V_{max}
mPG
AVA
AFFM
C
FCN
$\hat{y}$
y
L_{cls}
DLi-ASc
Main Task
Auxiliary Task
Weighted Fusion
V_{max}
$Z_{V_{max}}$
$L_{V_{max}}$
$\hat{y}$
y
$\sigma(f_{weight}(x))$
$w_{V_{max}}$
mPG
Z_{mPG}
L_{mPG}
$\hat{y}$
y
$\sigma(f_{weight}(x))$
w_{mPG}
C
Z_{fused}
AVA
Z_{AVA}
L_{AVA}
$\hat{y}$
y
$\sigma(f_{weight}(x))$
w_{AVA}
Auxiliary Task
Auxiliary Loss
AFFM

Supplemental Methods 4. Cutoff of DLi-ASc for Each AS Severity Category

We derived the DLi-ASc cutoffs by calculating the mean values of DLi-ASc across normal, AV sclerosis, mild, moderate, and severe AS groups in the validation dataset. To establish cutoff points, we took the midpoint between the mean DLi-ASc values of each consecutive AS severity category. For example, the mean DLi-ASc values for moderate and severe AS were 59.1 and 80.3, respectively, yielding a cutoff of 69.7 for diagnosing severe AS. This approach resulted in the following DLi-ASc cutoffs: 24.6 for AV sclerosis, 45.4 for mild AS, 53.7 for moderate AS, and 69.7 for severe AS.

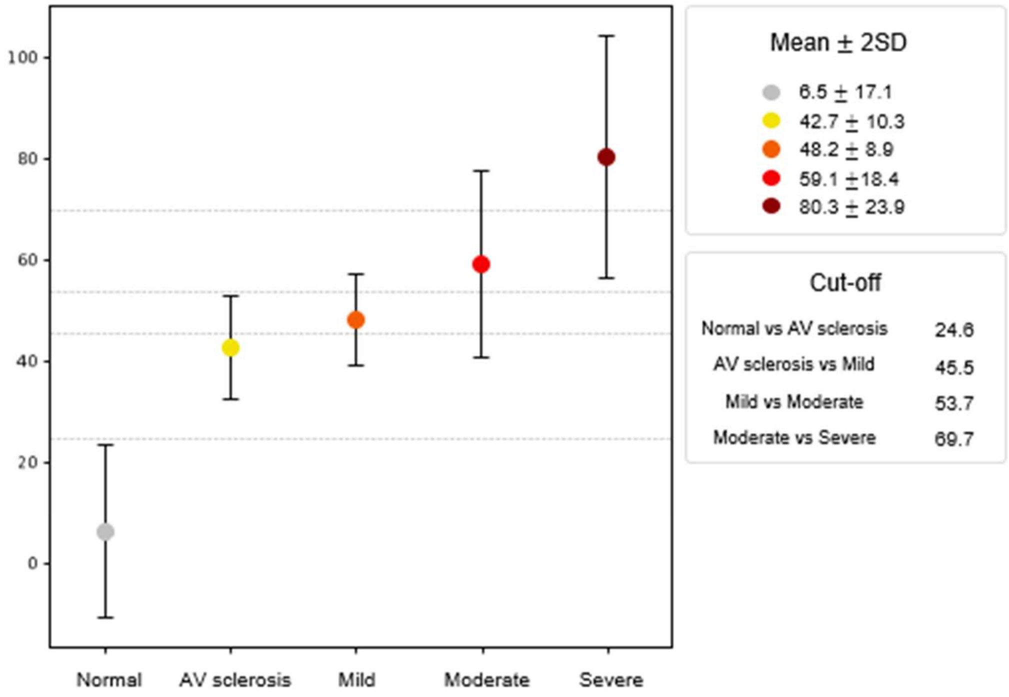

Supplemental Methods 5. Automated Conventional AVA Assessment Algorithm

Supplemental Methods 5.1. Automatic Measurement of Spectral Doppler Echocardiography

The Doppler segmentation network employs the BiSeNetV2 architecture, which has been thoroughly described in our previous publication.[4-6] The BiSeNetV2 is specifically designed to balance accuracy and computational efficiency, making it suitable for real-time applications. During the training process, the network was optimized using standard cross-entropy loss. Notably, our Doppler segmentation network did not include training data for the AV continuous wave (CW) Doppler from the right parasternal view. However, this view can be inferred as a vertically flipped version of the CW Doppler AV in the apical view. During inference, we preprocess the input by flipping the image vertically before running it through the network, allowing us to utilize the same trained model for both views without additional training data.[6]

AV CW Doppler from apical and right parasternal view

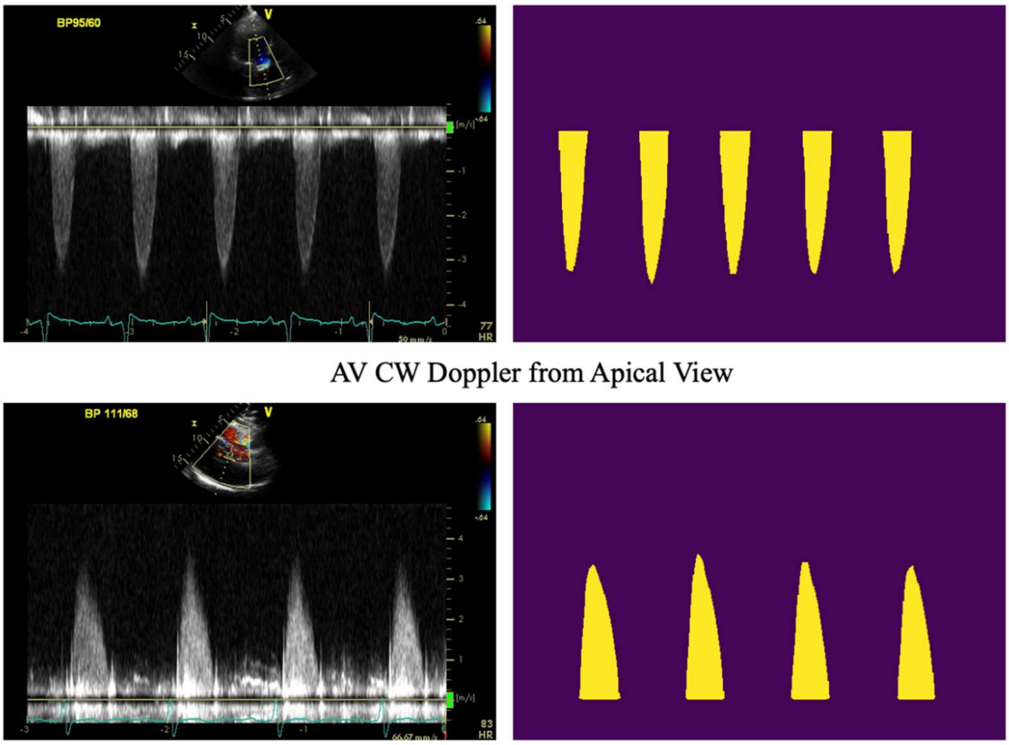

AV CW Doppler from Apical View

AV CW Doppler from Right Parasternal View

For spectral Doppler images, AV V_{max} and VTI were derived from the segmented Doppler envelope of AV CW Doppler. This analysis included AV CW Doppler obtained from both the apical and right parasternal views, selecting the largest envelope across all cycles in all images to obtain AV V_{max} and VTI, aiming to prevent underestimation of AS jet velocity. The LVOT PW Doppler analysis also spanned all cycles, using the average value of LVOT VTI to avoid overestimating LVOT flow.[7] These measurements were then used to calculate mPG and AVA, which were used to assess the presence and severity of AS.[8]

Supplemental Methods 5.2. Automated Measurement of LVOT Diameter

For the PLAX segmentation network, we utilized the SegFormer architecture, which includes a transformer encoder that provides multiscale features without needing positional encoding and a lightweight multi-layer perceptron (MLP) decoder integrating local and global attention for efficient segmentation.[9] A weighted cross-entropy loss was applied during training to account for the relatively small size of the mitral valve (MV) and AV in the PLAX view. A total of 2,369 PLAX videos were annotated at four key frames in the cardiac cycle: end-diastole, mid-systole, end-systole, and mid-diastole. Three experienced sonographers – MJ Jung and A Choi (each with 20 years in the field) and AR Kim (with 10 years) – performed the annotations. All segmentations were subsequently reviewed by SA Lee, a cardiologist specializing in echocardiography, with 10 years of experience. The images were resized into 512 × 512 and normalized to [-1,1]. We used the Adam optimizer with a learning rate of 0.001 and incorporated RandAug, enhanced with echocardiography-specific augmentations such as shadow, depth attenuation, and haze, to improve model robustness.[10, 11] Additionally, a cosine annealing learning rate schedule was employed to optimize the training process.[12] Complete videos are presented in **Video S1**.

Human Expert Annotation and AI Predicted Mask in PLAX View

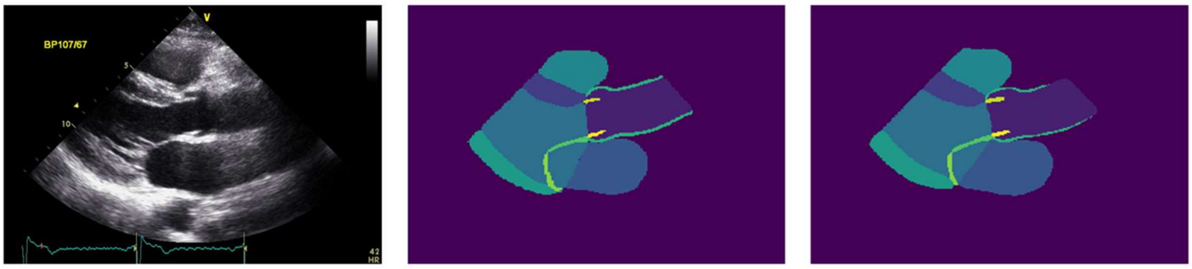

Input Video

Groundtruth

Prediction

From the predicted segmentation mask, we identify points where the MV intersects with the aorta and where the septum intersects with the aorta to determine annulus points. Using these points, we measure the LVOT diameter at three locations: 1) at the annulus, 2) 2.5mm away from the annulus towards the LV cavity, and 3) 5mm away from the annulus towards the LV cavity. This approach reflects differing opinions on the appropriate location for measuring the LVOT diameter.[8] Complete videos are presented in **Video S1**.

Automatic LVOT Measurements From the Predicted Segmentation Mask

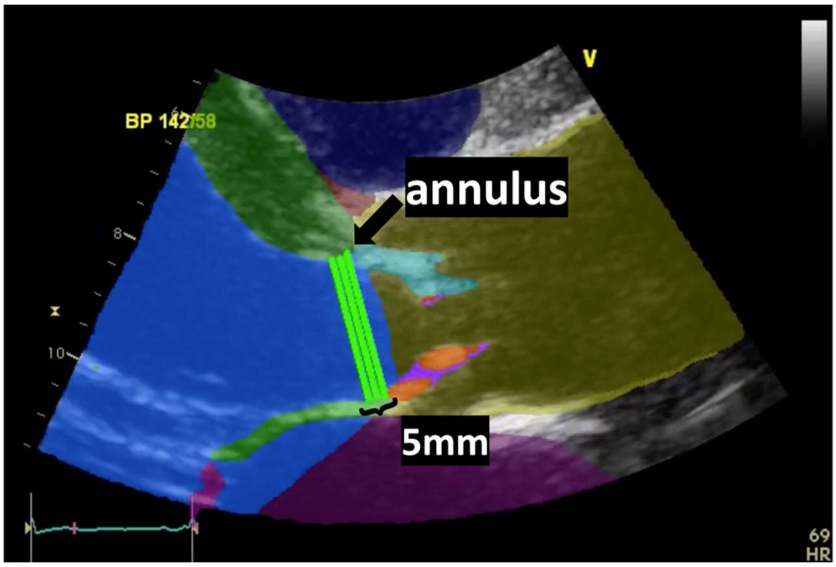

Supplemental Methods 6. Quantifying Uncertainty in Predicted Segmentation

Quantifying uncertainty in segmentation predictions is a meticulous process, crucial because segmentation errors can significantly impact the accuracy of subsequent automatic measurements. This uncertainty arises from two primary sources: epistemic uncertainty, which arises from a lack of knowledge of the DL model, and aleatoric uncertainty, which results from inherent noise in the data. To quantify these uncertainties, we calculate predictive entropy from the segmentation network's probability map, which provides a measure of the total uncertainty by combining both aleatoric and epistemic uncertainties. The entropy is computed for each pixel in the segmentation map, allowing us to identify regions with high uncertainty. The entropy is calculated using the equation:

$$H[\boldsymbol{p_{ij}}] = \sum_c p_{ij}^c \log p_{ij}^c,$$

where i, j represent pixel coordinates and c represents the class.

For quantifying uncertainty in the LVOT measurements in the PLAX view, we focus on regions of interests (ROIs) that directly affect the performance of LVOT measurement. Using the detected two points marking the annulus, we set a 50 × 50 ROI (10% of the resized image) centered on these points, as shown in the figure below**.** We then summed the entropy of each pixel within this ROI to assess uncertainty. For Doppler measurements, we evaluated uncertainty for the Doppler signal in each single beat. With the detected significant Doppler flow, we create an ROI and crop the entropy map to the corresponding ROI, normalizing it to 64 × 64. By summing the entropy values within the normalized ROI, we obtain the quantified uncertainty for each Doppler signal by beat. Complete videos are presented in **Video S2**.

Regions of Interest marked for assessing uncertainty

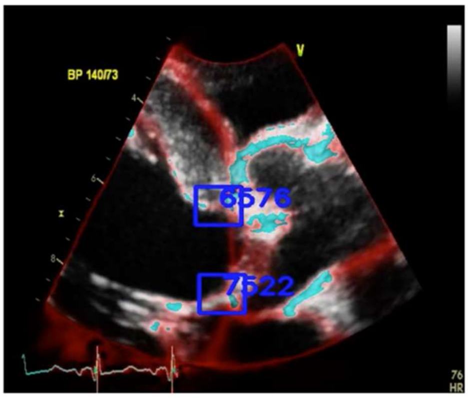

PLAX zoomed AV

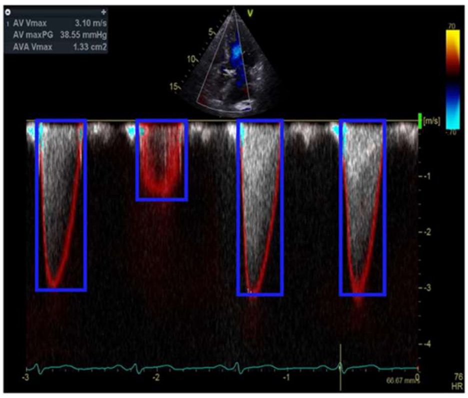

CW Doppler AV

From the validation set used for training, we find thresholds to reject the frames or beats by identifying the top percentage of frames or beats with the highest uncertainty. Specifically, we reject the top 5% of frames with the highest uncertainty from PLAX AV zoomed videos and the top 1% of beats with the highest uncertainty from Doppler images. We calculate the mean of entropy scores and add 1.96 × s.d. for PLAX frames and 2.33 × s.d. for Doppler images. The distributions of the entropy scores for both PLAX and Doppler images are shown in the figure below, illustrating how the thresholds are set.

Distribution of Entropy Scores

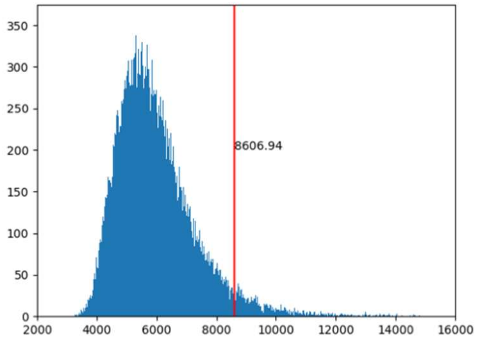

PLAX zoomed AV

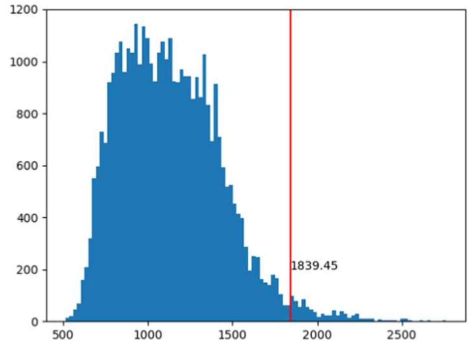

Doppler

Samples with High Uncertainty Identified through Entropy Scores

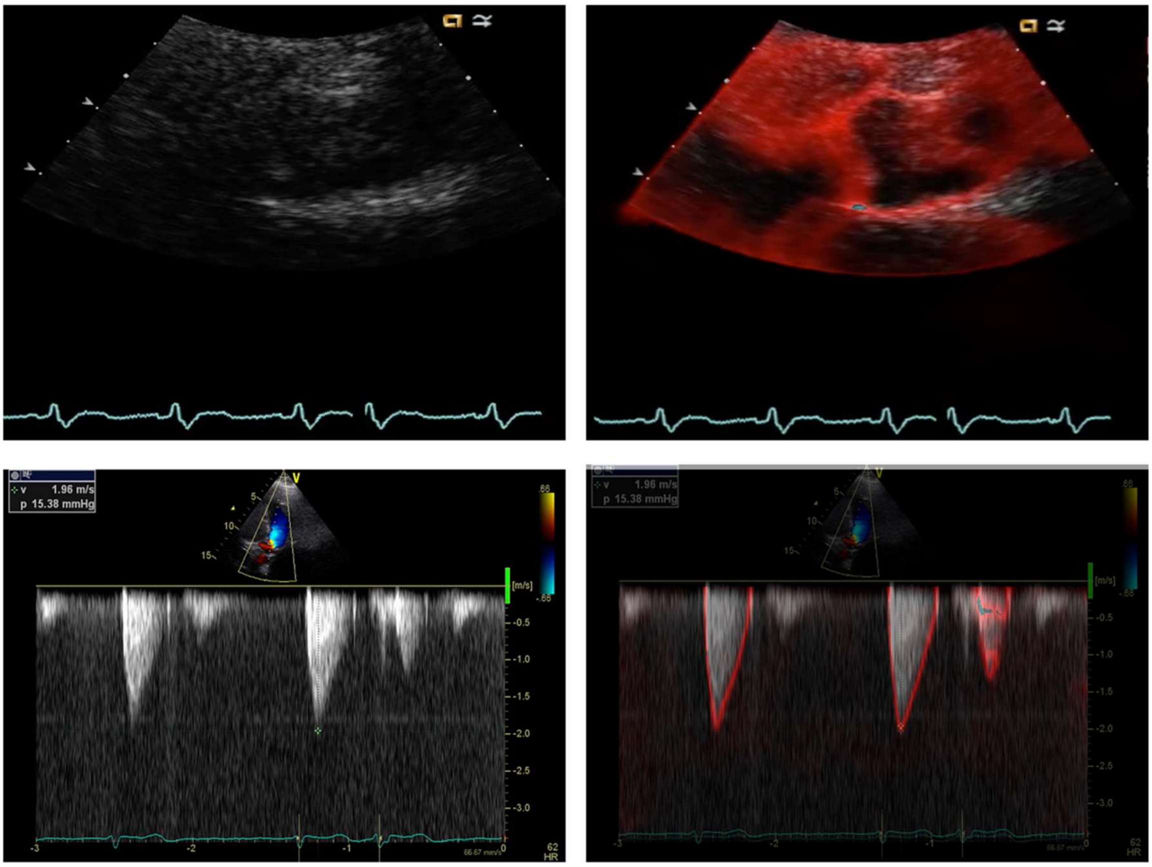

The figure above displays examples of Doppler and B-Mode images that were filtered out due to high uncertainty. These samples belong to the right end of the uncertainty distribution, representing the top percentage of frames and beats with the highest entropy scores. The highlighted regions in these images show areas of significant uncertainty, which were excluded from further analysis to ensure the accuracy of the automatic measurements. For spectral Doppler, the in/out filter was applied on a cardiac cycle basis. As seen in the AV CW Doppler image, the first two cycles were analyzed normally due to low uncertainty, while the last cycle was excluded due to high uncertainty.

Supplemental Methods 7. Validation of LVOT Diameter Measurement

To assess the accuracy of the LVOT diameter automatic measurement, part of our AI-based system (Sonix Health, Ontact Health, Korea), we conducted a validation study with 212 American patients who underwent echocardiographic examination at Mayo Clinic Arizona, USA and Severance Hospital in Seoul, Korea. Considering the inherent variability in LVOT measurements, both AI and manual measurements were taken on the same view and frame. The AI system measured the LVOT diameter at three specific points: the annulus, 2.5mm from the annulus towards the LV side, and 5mm from the annulus, all marked in fluorescent green. Manual measurements were conducted at the annulus (dark red) and 5mm from the annulus (dark green) for comparison. The association between automated and manual measurements was assessed using the Spearman correlation analysis (r) and mean absolute error (MAE).

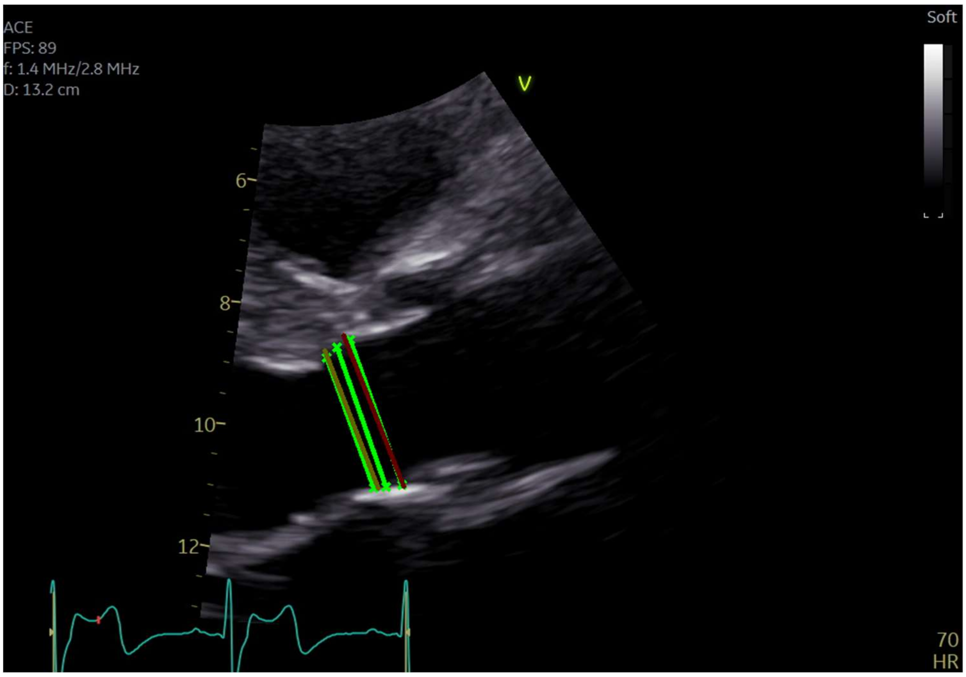

Comparison	**LVOT Measurement Location**	**r**	**MAE (cm)**
Manual vs Manual	Annulus - 5mm from Annulus	0.931	0.091
Manual vs AI	Annulus - Annulus	0.913	0.116
	Annulus - 2.5mm from Annulus	0.904	0.114
	Annulus - 5mm from Annulus	0.884	0.144
	5mm from Annulus - Annulus	0.909	0.148
	5mm from Annulus - 2.5mm from Annulus	0.948	0.114
	5mm from Annulus - 5mm from Annulus	0.948	0.114

Our AI system provides LVOT diameter measurements at three locations. To determine which value to use for AVA calculation in this study, we compared the AI measurement at each location to prior manual measurements within the training set. Results showed that the automated measurement at the annulus had the highest correlation with manual measurement and lowest mean absolute error (MAE), leading us to select the annuus measurement for AVA calculation.

LVOT at the annulus

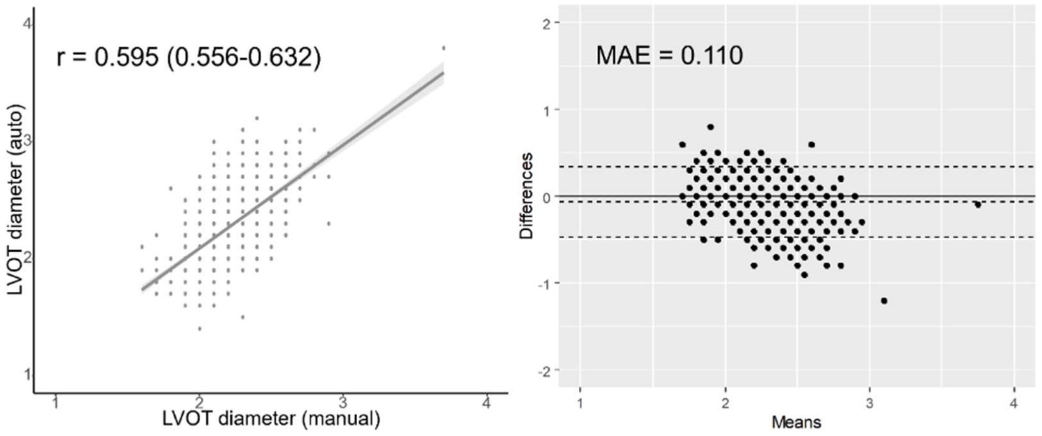

LVOT 2.5mm away from the annulus

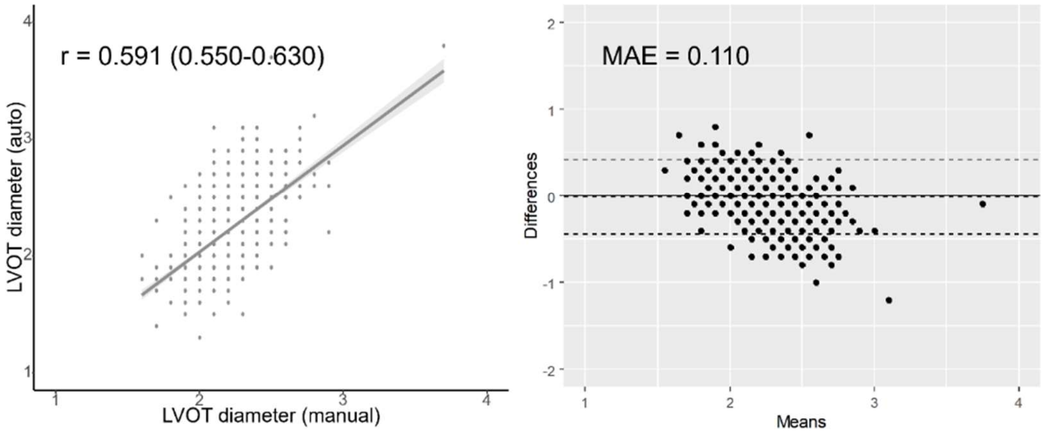

LVOT 5mm away from the annulus

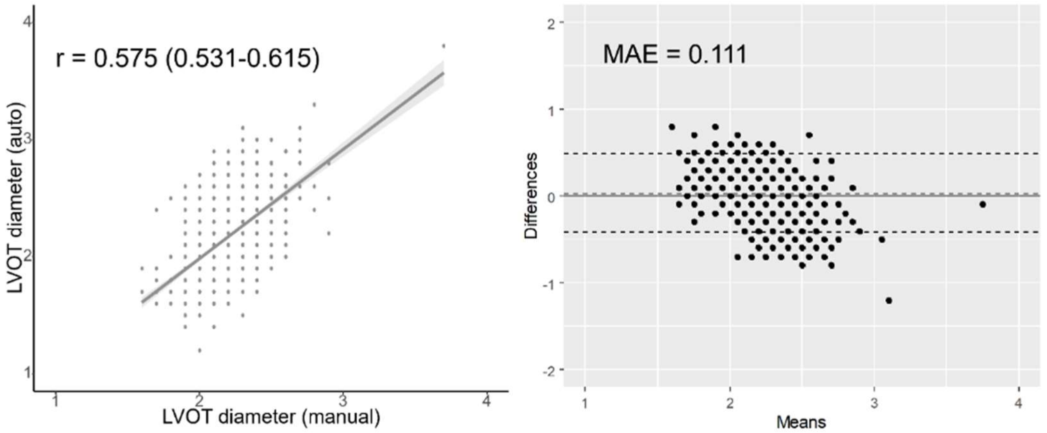

Supplemental Methods 8. Availability of Ground Truth Measurements and Success Rate of Auto-Measurements in the AS Group

The availability of ground truth measurements and the success rate of our algorithm's auto-measurements in the AS group are as follows.

	Ground truth	**Auto-measurement**	**Matching case**
	(% of the overall case)	**(% of the overall case)**	**(% of available GT cases)**
ITDS (n=328)			
AV Vmax	328 (100)	328 (100)	328 (100)
AV mPG	320 (97.6)	328 (100)	320 (100)
LVOT VTI	166 (50.6)	164 (50.0)	164 (98.8)
LVOT diameter	159 (48.5)	290 (88.4)	141 (88.7)
AVA	156 (47.6)	143 (43.6)	133 (85.3)
DHDS (n=659)			
AV Vmax	83 (12.6)	652 (98.9)	83 (100)
AV mPG	602 (91.4)	652 (98.9)	598 (99.3)
LVOT VTI	438 (66.5)	583 (88.5)	367 (83.8)
LVOT diameter	425 (64.5)	618 (93.8)	405 (95.3)
AVA	560 (85.0)	543 (82.4)	457 (81.6)
TDDS (n=443)			
AV Vmax	443 (100)	443 (100)	443 (100)
AV mPG	440 (99.3)	443 (100)	440 (100)
LVOT VTI	235 (53.0)	233 (52.6)	233 (99.1)
LVOT diameter	228 (51.5)	419 (94.6)	212 (93.0)
AVA	227 (51.2)	219 (48.8)	209 (96.5)

AV, aortic valve; AVA, aortic valve area; LVOT, left ventricle outflow tract; mPG, mean pressure gradient; V_{max}, peak aortic valve velocity; VTI, velocity time integral.

Supplemental Results 1. View Classification Performance in Each Dataset

In this study, view classifications performance was assessed based on the framework's ability to accurately identify views necessary for AS evaluation. All other echocardiographic views are categorized as "Other", as they do not directly contribute to AS evaluation within our framework.

ITDS

	n	Precision	Recall (Sensitivity)	specificity	F1-score	Accuracy
PLAX-LV	1,525	0.985 (0.985, 0.989)	0.991 (0.991, 0.995)	1.000 (1.000, 1.000)	0.988 (0.984, 0.992)	0.996 (0.996, 0.996)
PLAX zoomed AV	197	0.985 (0.984, 1.000)	0.685 (0.685, 0.711)	0.999 (0.999, 0.999)	0.807 (0.757, 0.852)	
PLAX zoomed AV & MV	663	0.896 (0.896, 0.904)	0.979 (0.979, 0.987)	1.000 (1.000, 1.000)	0.936 (0.924, 0.948)	
PSAX, level of great vessels	1,819	0.990 (0.990, 0.994)	0.971 (0.971, 0.974)	0.999 (0.999, 0.999)	0.980 (0.976, 0.985)	
PW Doppler LVOT	886	0.965 (0.965, 0.971)	0.998 (0.998, 1.000)	1.000 (1.000, 1.000)	0.981 (0.975, 0.987)	
CW Doppler AV from Apical Views	1,282	0.914 (0.914, 0.918)	0.966 (0.966, 0.970)	1.000 (1.000, 1.000)	0.939 (0.930, 0.949)	
CW Doppler AV from the right parasternal view	38	0.864 (0.861, 0.977)	1.000 (0.995, 1.000)	1.000 (1.000, 1.000)	0.928 (0.874, 0.975)	
other	74,885	0.999 (0.999, 0.999)	0.998 (0.998, 0.998)	0.986 (0.986, 0.987)	0.998 (0.998, 0.998)	

AV, aortic valve; CW, continuous wave Doppler; ITDS, internal test dataset; LVOT, left ventricle outflow tract; MV, mitral valve; PLAX, parasternal long-axis view. PSAX, parasternal short-axis view; PW, pulsed wave Doppler

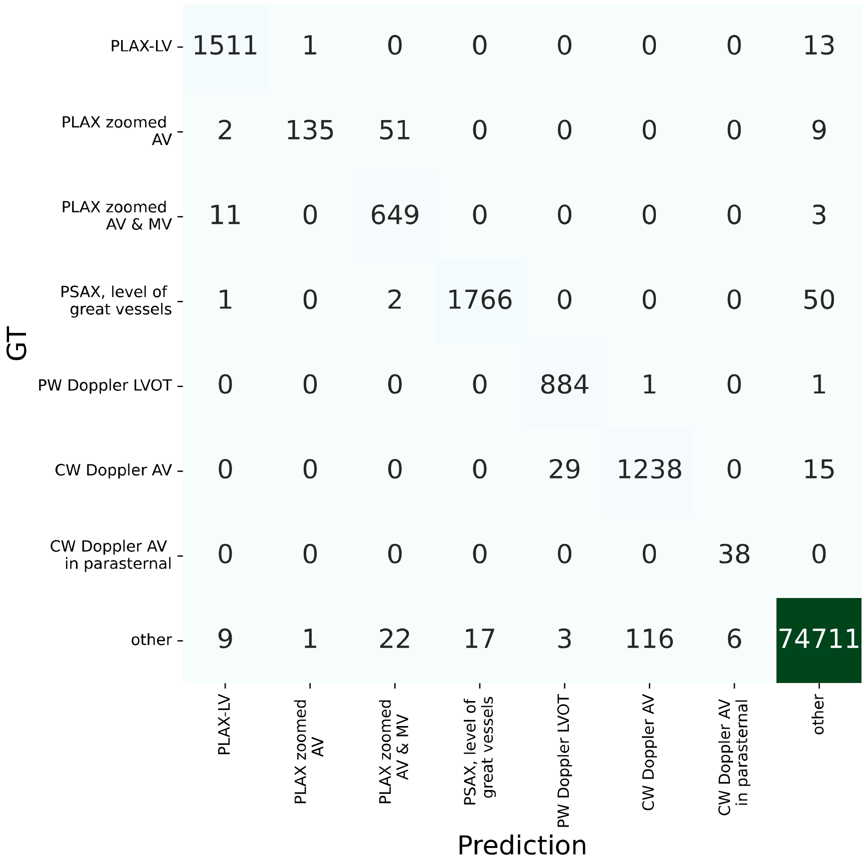

	PLAX-LV	PLAX zoomed AV	PLAX zoomed AV & MV	PSAX, level of great vessels	PW Doppler LVOT	CW Doppler AV	CW Doppler AV in parasternal	other
PLAX-LV	1511	1	0	0	0	0	0	13
PLAX zoomed AV	2	135	51	0	0	0	0	9
PLAX zoomed AV & MV	11	0	649	0	0	0	0	3
PSAX, level of great vessels	1	0	2	1766	0	0	0	50
PW Doppler LVOT	0	0	0	0	884	1	0	1
CW Doppler AV	0	0	0	0	29	1238	0	15
CW Doppler AV in parasternal	0	0	0	0	0	0	38	0
other	9	1	22	17	3	116	6	74711

DHDS

	n	Precision	Recall (Sensitivity)	specificity	F1-score	Accuracy
PLAX-LV	3280	0.971 (0.971, 0.973)	0.998 (0.998, 1.000)	1.000 (1.000, 1.000)	0.984 (0.981, 0.987)	0.995 (0.995, 0.995)
PLAX zoomed AV	1313	0.989 (0.989, 0.994)	0.909 (0.909, 0.914)	0.999 (0.999, 0.999)	0.947 (0.938, 0.956)	
PLAX zoomed AV & MV	89	0.510 (0.509, 0.540)	0.876 (0.875, 0.935)	0.998 (0.998, 0.998)	0.645 (0.589, 0.702)	
PSAX, level of great vessels	3040	0.947 (0.947, 0.949)	0.994 (0.994, 0.996)	1.000 (1.000, 1.000)	0.970 (0.966, 0.974)	
PW Doppler LVOT	2182	0.999 (0.999, 1.000)	0.998 (0.998, 1.000)	1.000 (1.000, 1.000)	0.998 (0.997, 1.000)	
CW Doppler AV from Apical Views	2275	0.987 (0.986, 0.989)	0.968 (0.968, 0.970)	0.999 (0.999, 0.999)	0.977 (0.973, 0.982)	
CW Doppler AV from the right parasternal view	20	0.810 (0.804, 1.000)	0.850 (0.843, 1.000)	1.000 (1.000, 1.000)	0.832 (0.711, 0.930)	
other	92460	0.998 (0.998, 0.998)	0.997 (0.997, 0.997)	0.987 (0.987, 0.987)	0.997 (0.997, 0.998)	

AV, aortic valve; CW, continuous wave Doppler; DHDS, Distinct Hospital Dataset; LVOT, left ventricle outflow tract; MV, mitral valve; PLAX, parasternal long-axis view. PSAX, parasternal short-axis view; PW, pulsed wave Doppler

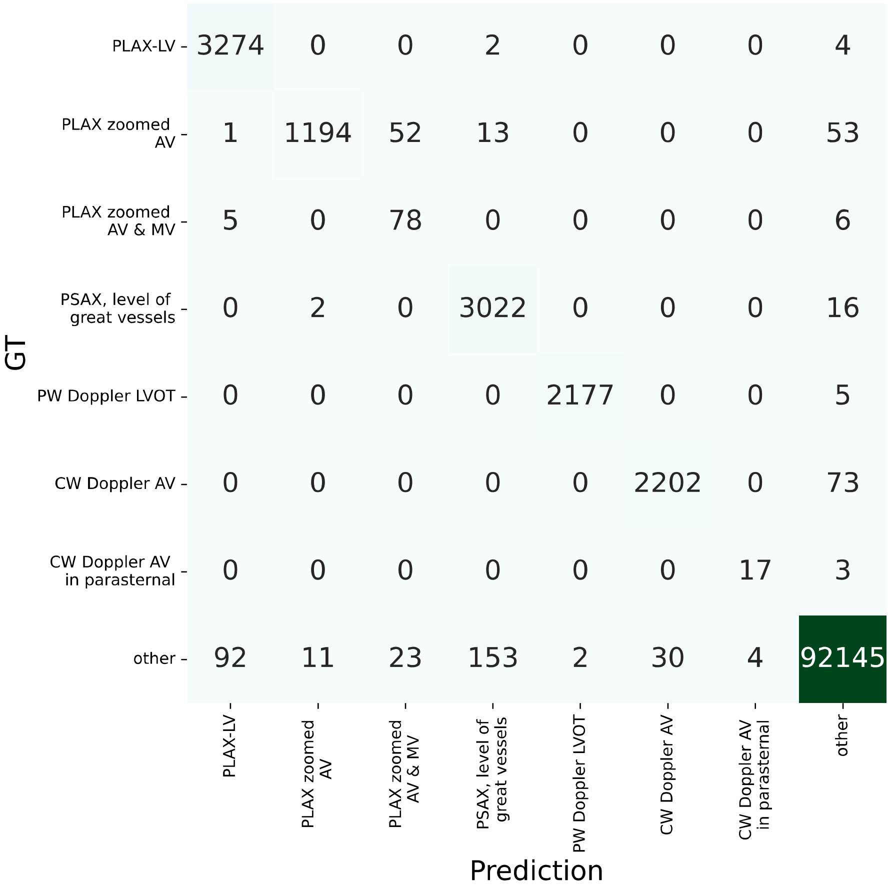
GT
Prediction

	PLAX-LV	PLAX zoomed AV	PLAX zoomed AV & MV	PSAX, level of great vessels	PW Doppler LVOT	CW Doppler AV	CW Doppler AV in parasternal	other
PLAX-LV	3274	0	0	2	0	0	0	4
PLAX zoomed AV	1	1194	52	13	0	0	0	53
PLAX zoomed AV & MV	5	0	78	0	0	0	0	6
PSAX, level of great vessels	0	2	0	3022	0	0	0	16
PW Doppler LVOT	0	0	0	0	2177	0	0	5
CW Doppler AV	0	0	0	0	0	2202	0	73
CW Doppler AV in parasternal	0	0	0	0	0	0	17	3
other	92	11	23	153	2	30	4	92145

TDDS

	n	Precision	Recall (Sensitivity)	specificity	F1-score	Accuracy
PLAX-LV	1377	0.984 (0.984, 0.988)	0.992 (0.992, 0.996)	1.000 (1.000, 1.000)	0.988 (0.984, 0.992)	0.994 (0.994, 0.994)
PLAX zoomed AV	193	0.907 (0.905, 0.968)	0.404 (0.404, 0.428)	0.998 (0.998, 0.998)	0.560 (0.491, 0.625)	
PLAX zoomed AV & MV	683	0.840 (0.840, 0.847)	0.993 (0.992, 1.000)	1.000 (1.000, 1.000)	0.910 (0.900, 0.921)	
PSAX, level of great vessels	1829	0.995 (0.995, 0.999)	0.948 (0.948, 0.951)	0.998 (0.998, 0.998)	0.971 (0.965, 0.976)	
PW Doppler LVOT	833	1.000 (1.000, 1.000)	1.000 (1.000, 1.000)	1.000 (1.000, 1.000)	1.000 (1.000, 1.000)	
CW Doppler AV from Apical Views	1670	0.905 (0.905, 0.908)	0.992 (0.992, 0.995)	1.000 (1.000, 1.000)	0.946 (0.939, 0.954)	
CW Doppler AV from the right parasternal view	88	0.917 (0.915, 0.972)	1.000 (0.998, 1.000)	1.000 (1.000, 1.000)	0.956 (0.926, 0.983)	
other	67453	0.998 (0.998, 0.998)	0.997 (0.997, 0.997)	0.981 (0.981, 0.982)	0.997 (0.997, 0.998)	

AV, aortic valve; CW, continuous wave Doppler; TDDS, Temporally Distinct Dataset; LVOT, left ventricle outflow tract; MV, mitral valve; PLAX, parasternal long-axis view. PSAX, parasternal short-axis view; PW, pulsed wave Doppler

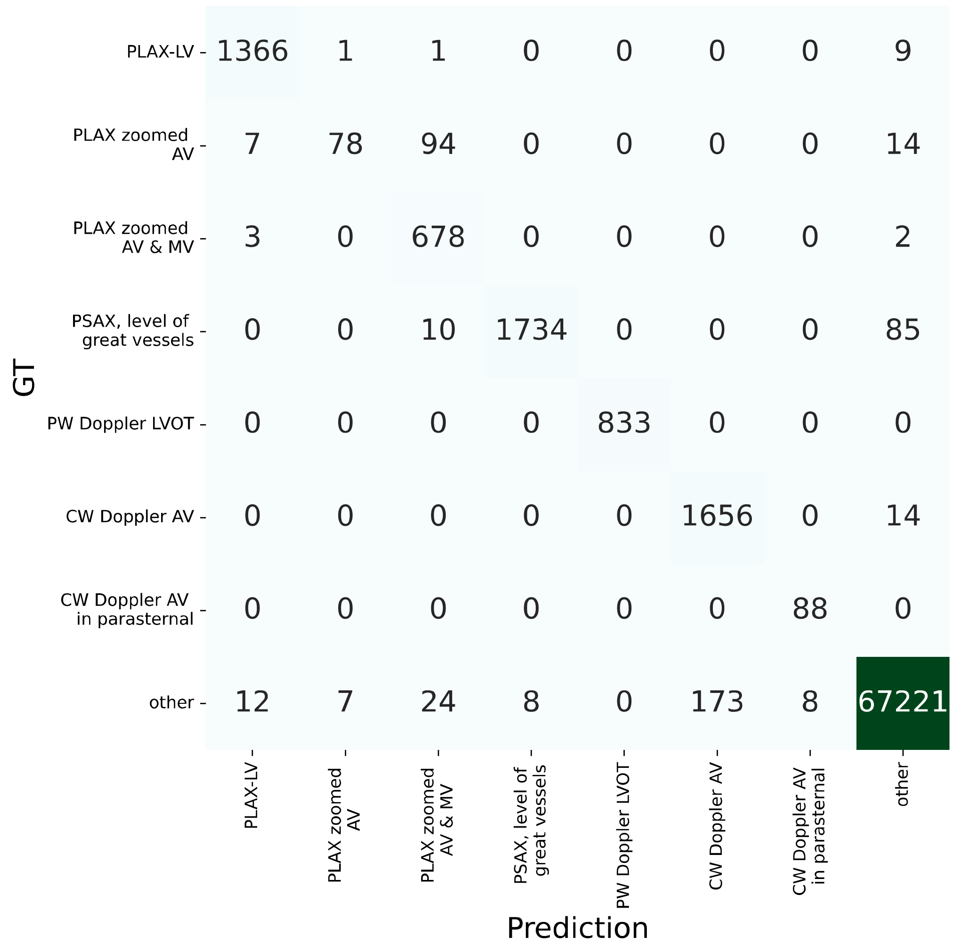

	PLAX-LV	PLAX zoomed AV	PLAX zoomed AV & MV	PSAX, level of great vessels	PW Doppler LVOT	CW Doppler AV	CW Doppler AV in parasternal	other
PLAX-LV	1366	1	1	0	0	0	0	9
PLAX zoomed AV	7	78	94	0	0	0	0	14
PLAX zoomed AV & MV	3	0	678	0	0	0	0	2
PSAX, level of great vessels	0	0	10	1734	0	0	0	85
PW Doppler LVOT	0	0	0	0	833	0	0	0
CW Doppler AV	0	0	0	0	0	1656	0	14
CW Doppler AV in parasternal	0	0	0	0	0	0	88	0
other	12	7	24	8	0	173	8	67221

Supplemental Results 2. Distribution of DLi-ASc According to Conventional AS Parameters

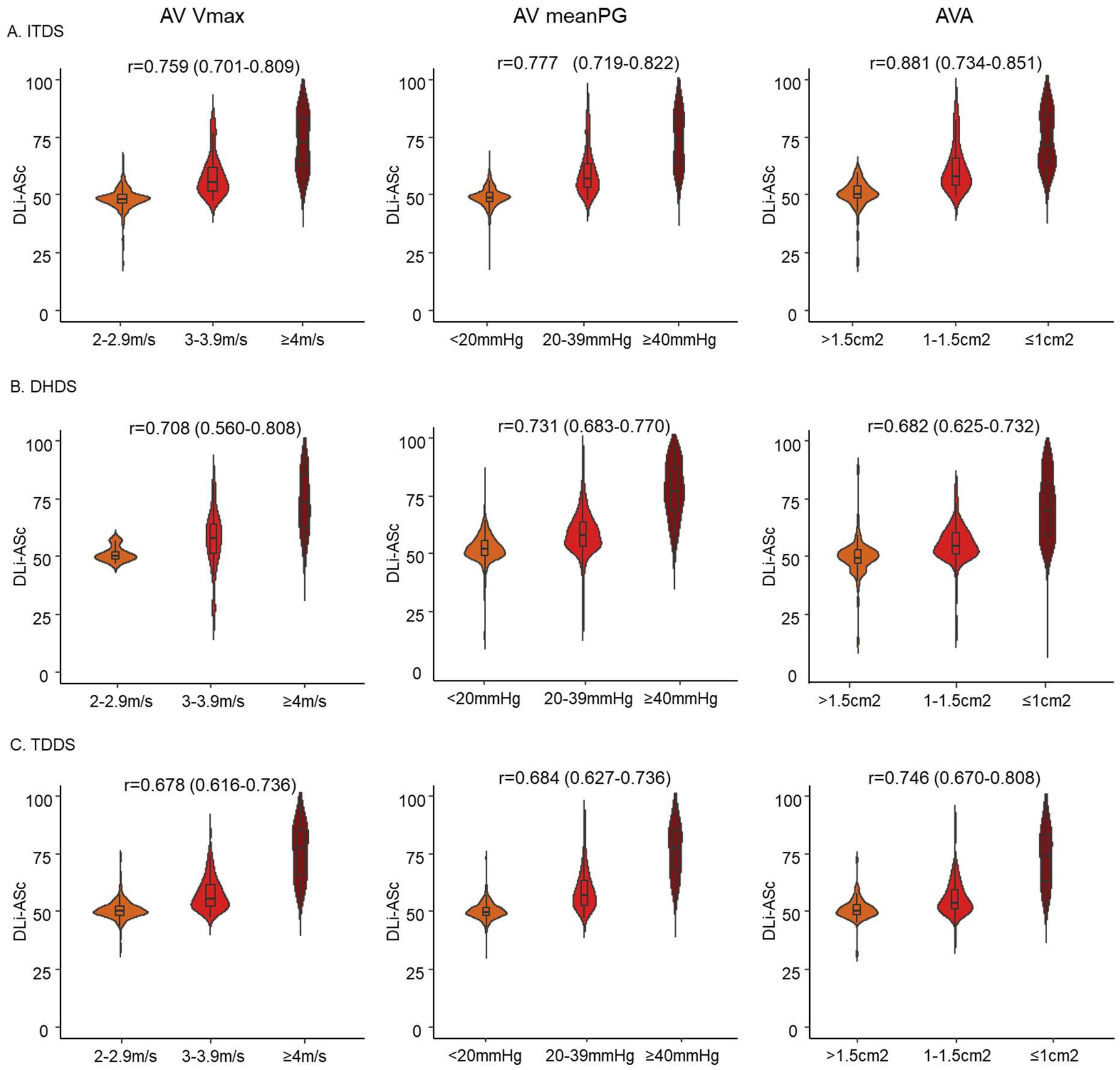

Supplemental Results 3. Distribution of DLi-ASc in Discordant Cases of AS Severity

In this study, discordant cases were defined as those where AV V_{max}, mPG, and AVA did not consistently fall into a single AS severity class, resulting in interpretations spanning two classes, such as mild to moderate, moderate to severe, or cases of low-flow, low-gradient AS where reduced stroke volume results in a lower pressure gradient despite significant stenosis. These cases were excluded from training, validation, and testing in the DDS. However, when included in the internal test dataset (ITDS) for comparison, the distribution of DLi-ASc was as follows. This result suggests that DLi-ASc can be helpful in cases where traditional parameters are discordant, making the assessment of AS severity challenging.

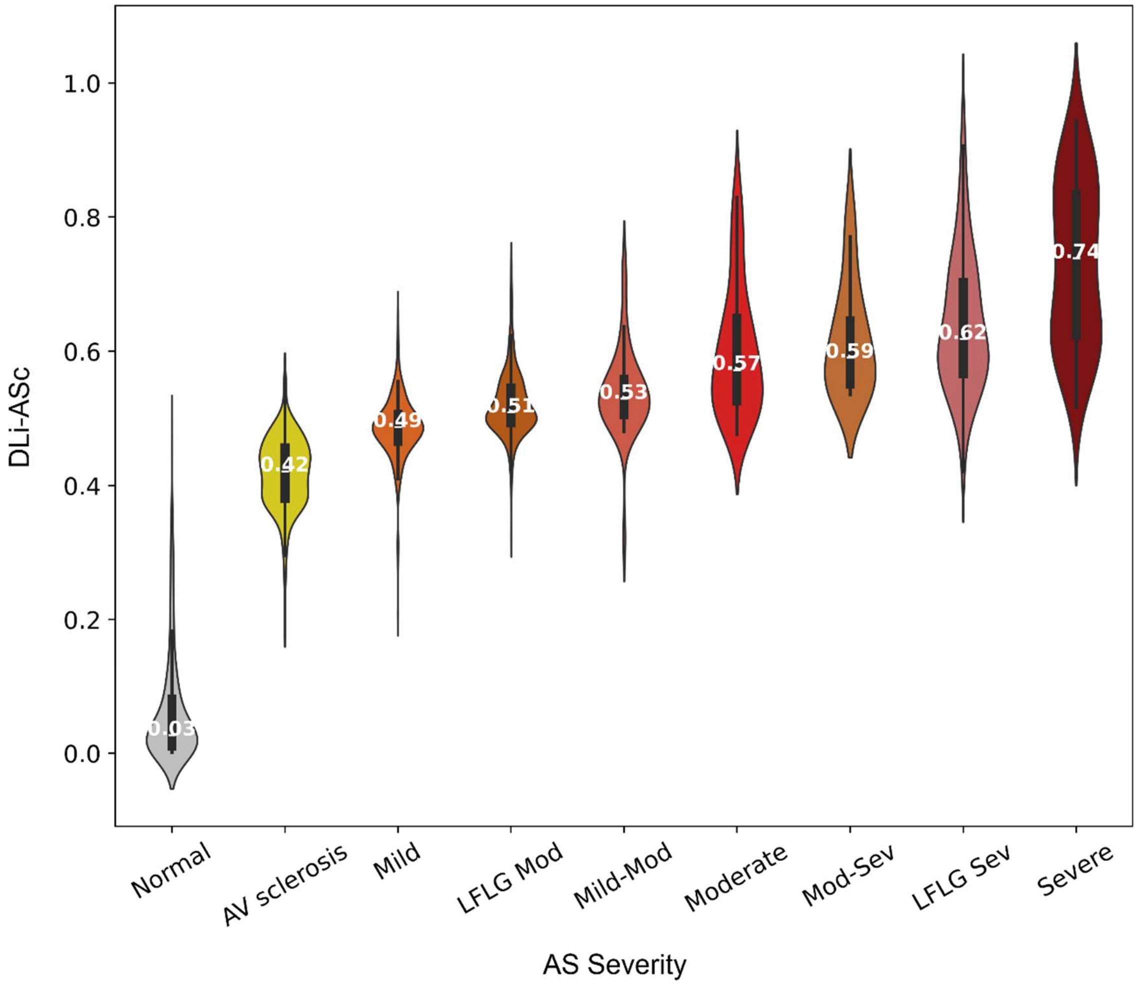

LFLG Mod, low-flow low-gradient moderate aortic stenosis; LFLG Sev, low-flow low-gradient severe aortic stenosis

Supplemental Results 4. Discrimination of Low Flow Low Gradient Severe AS using DLi-ASc

DHDS

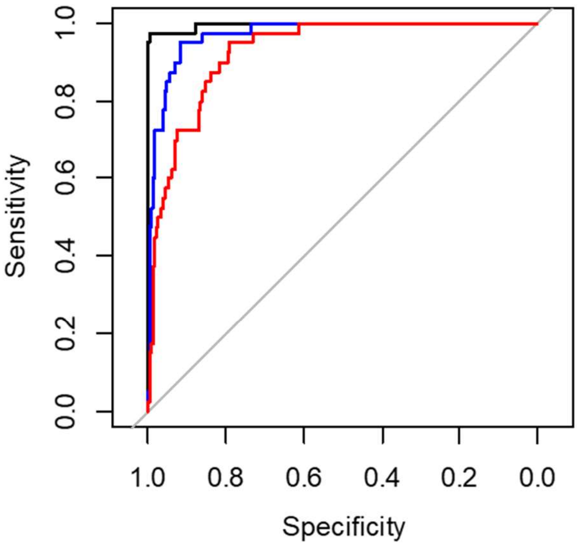

	AUC (95% CI)
Normal AV vs. LFLG severe AS	0.997 (0.991-0.999)
Normal to mild AV vs. LFLG severe AS	0.974 (0.958-0.989)
Normal to mod AV vs. LFLG severe AS	0.930 (0.902-0.958)

TDDS

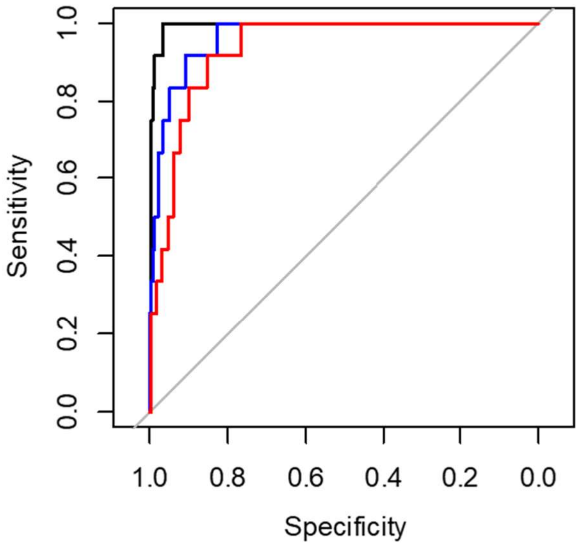

	AUC (95% CI)
Normal AV vs. LFLG severe AS	0.994 (0.987-0.999)
Normal to mild AV vs. LFLG severe AS	0.966 (0.936-0.996)
Normal to mod AV vs. LFLG severe AS	0.936 (0.895-0.976)

Supplemental Results 5. UMAP Visualization of AS Continuum Using Different Approaches

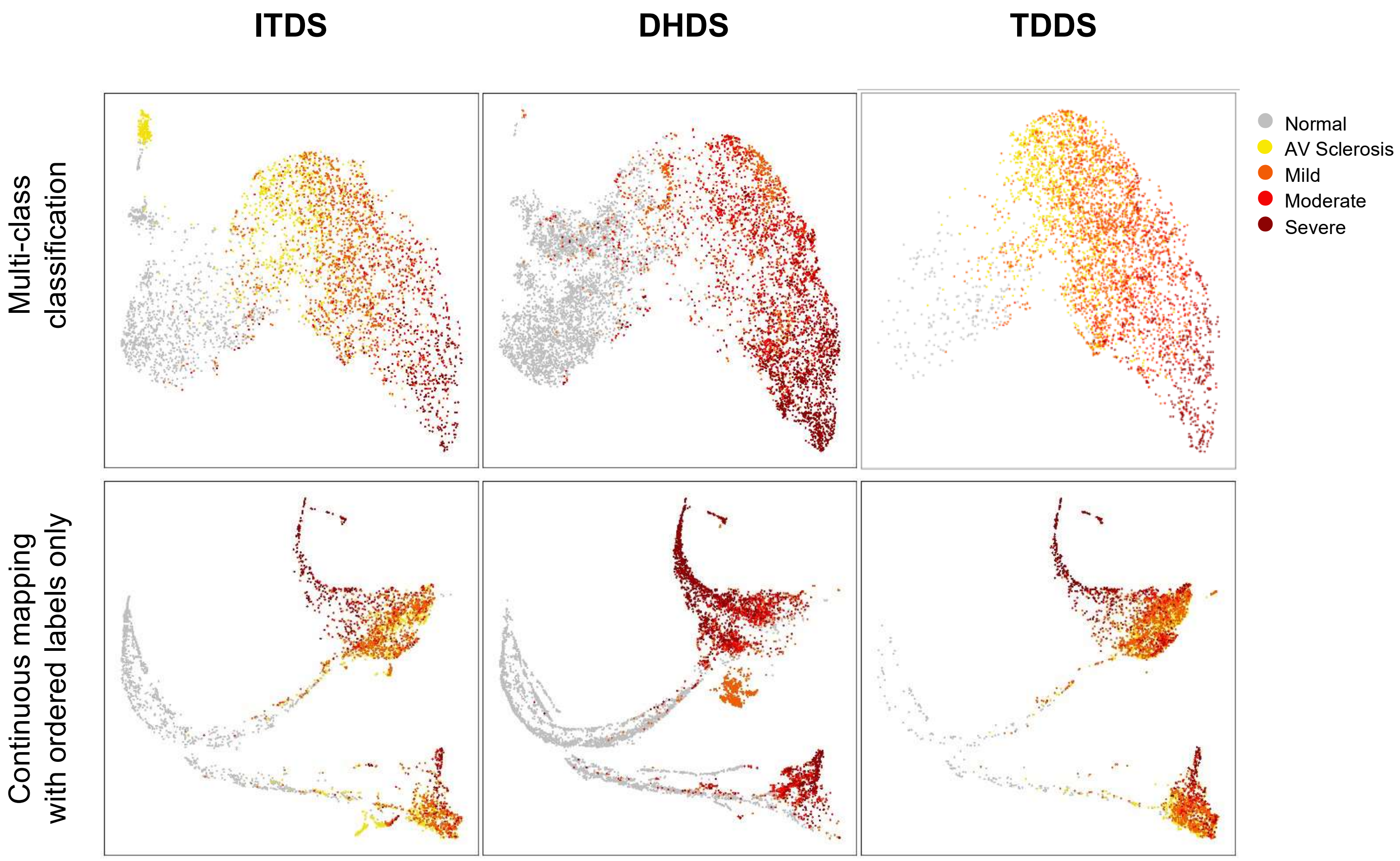

In the first row, multi-class classification uses standard 5-class cross-entropy loss with one-hot encoding. In the second row, the network is trained using only continuous mapping with ordered labels, without multi-task learning with auxiliary tasks.

Supplemental Results 6. Representative Failure Cases

The figure shows two representative cases where auto-measurement displayed significant discrepancies compared to manual measurement for AS parameters such as AV Vmax, mPG, and LVOT diameter.

In case A, measurement discrepancies in AV Vmax and mPG were attributed to ventricular bigeminy observed during AV Doppler measurement, leading to substantial beat-to-beat variability in the Doppler signal. For the manual measurement, AV Doppler was captured in a sinus rhythm, excluding premature beats, to ensure accuracy. In contrast, the auto-measurement processed all values in the AV CW Doppler signal and returned the highest value, resulting in the observed discrepancy. Despite this, both manual measurement and auto-measurement classified the case as severe AS. The estimated DLi-ASc Score was 87.2, further supporting the presence of severe AS.

In case B, there was a discrepancy in LVOT measurement due to differences in the measurement location. In manual evaluation, the measurement was taken slightly away from the aortic annulus toward the left ventricle, while the auto-measurement was performed closer to the annulus to determine the LVOT diameter. We previously evaluated various measurement points at different distances from the AV annulus in LVOT auto-measurement and found that measurement at the annulus level showed the highest correlation with the ground truth values (***Supplemental Methods*** *7*). However, in cases like this, where the LVOT demarcation is relatively unclear or the left ventricular septum is thick and sigmoid-shaped, the auto-measured LVOT value at the annulus level may be larger than usual. Nonetheless, both manual and automatic measurements classified the case as mild AS. The estimated DLi-ASc Score was 52.6, supporting the mild AS classification.

Case A: AV Vmax, AV mPG

Case B: LVOT diameter

Ground truth

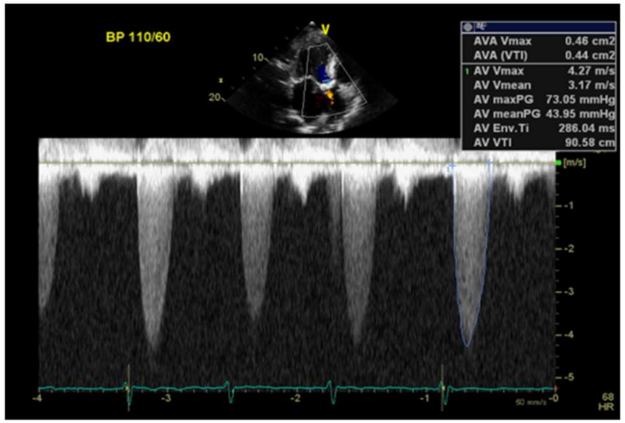

AVA Vmax	0.46 cm2
AVA (VTI)	0.44 cm2
1 AV Vmax	4.27 m/s
AV Vmean	3.17 m/s
AV maxPG	73.05 mmHg
AV meanPG	43.95 mmHg
AV Env.Ti	286.04 ms
AV VTI	90.58 cm

AV Vmax=4.3m/s, AV mPG=44mmHg

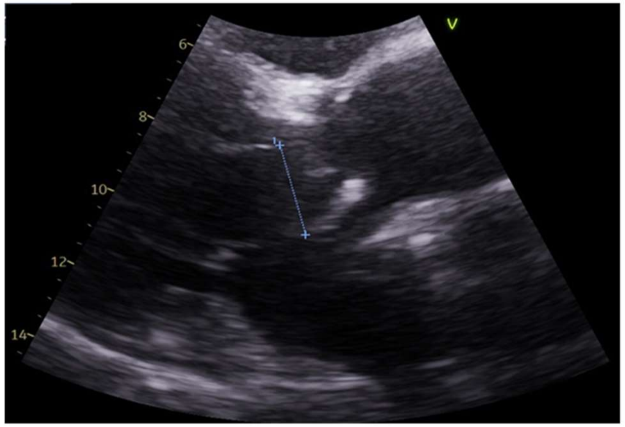

LVOT diameter=23mm

Auto-measured

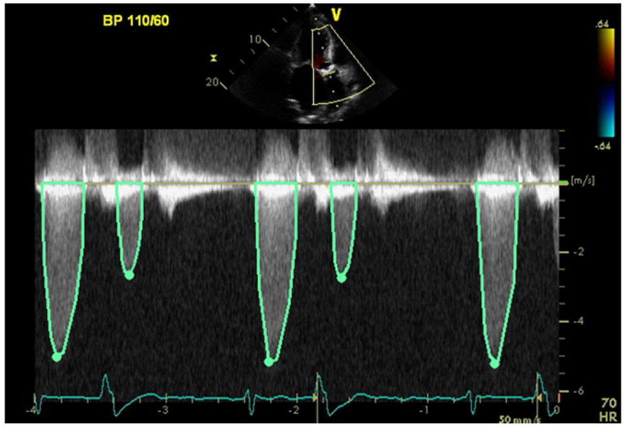

AV Vmax=5.6m/s, AV mPG=79mmHg

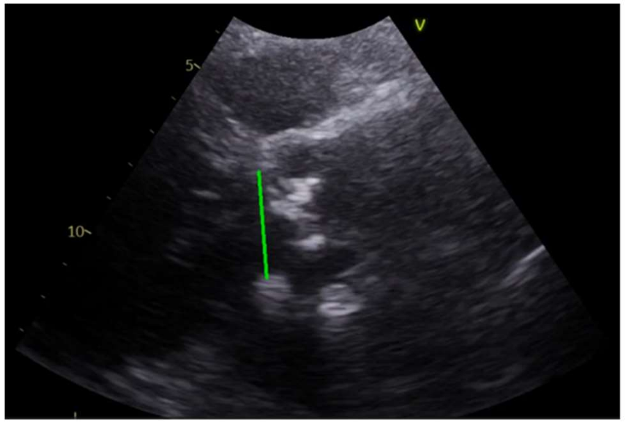

LVOT diameter=30mm

Supplemental Results 7. Comparative analysis with other existing studies

We compared our AI algorithm with those from prior studies, specifically those by Holste et al. and Wessler et al. Key difference between our model and these earlier approaches are as follows.

- **Model Architecture and Data Processing:** Holste et al.[3] utilized a 3D-ResNet 18 model with binary cross-entropy (BCE) loss for binary classification (non-severe vs. severe AS) on PLAX views, using 16 frames at a lower resolution (112 x 112). Additionally, Holste et al. used an ensemble of three models to improve robustness and classification accuracy. Wessler et al.[13], in contrast, employed a WideResNet28 model for three-category classification (no AS, early AS, significant AS) using a single frame from PLAX and/or PSAX views. Our model employs an R2Plus1D18 backbone, sampling 16 frames at a higher resolution (224 x 224), with a continuum-aware multi-task loss. This approach allows our model to capture both spatial and temporal features effectively, facilitating more nuanced AS severity assessment.
- **Loss Function:** Unlike the previous studies that use binary or categorical cross-entropy loss, our model leverages a continuum-aware multi-task loss. This custom loss function not only accommodates the progressive nature of AS by mapping ordered severity labels, but it also includes auxiliary regression tasks to predict key TTE parameters. This dual approach enables a more comprehensive and clinically relevant assessment of AS severity.
- **Target Classification:** Our model's focus on a five-class continuum-based AS assessment provides finer granularity compared to the binary classification by Holste et al. or the three-class system of Wessler et al. By aligning better with clinical practices, our model supports a more precise and ordered understanding of AS severity, which is crucial for guiding treatment decisions.

	Input type	Backbone	Loss	Required view	Sampled frame	Resolution	Target	Ensemble
Holste G et al.[3]	Video	3D-ResNet18	CrossEntropyLoss	PLAX	16	112 × 112	non severe AS, severe AS	Yes, 3 models
Wessler BS et al.[13]	Image	WideResNet28	CrossEntropyLoss	PLAX or/and PSAX	1	112 × 112	no AS, early AS, significant AS	No
DLi-ASc (Ours)	Video	R2Plus1D18	continuum-aware multi-task loss	PLAX or/and PSAX	16	224 × 224	Normal, AV sclerosis, Mild, Moderate, Severe	No

The results shown below demonstrated the performance advantages of our approach across multiple datasets (ITDS, DHDS, and TDDS). Our model consistently achieved higher accuracy for detecting any AS, significant AS, and severe AS across all datasets, underscoring the effectiveness of our continuum-based methodology.

	Holste G et al.[3]	Wessler BS et al.[13]	DLi-ASc (Ours)
ITDS			
any AS	0.844	0.859	0.958
significant AS	0.947	0.784	0.979
severe AS	0.972	-	0.985
DHDS			
any AS	0.946	0.967	0.996
significant AS	0.934	0.832	0.969
severe AS	0.958	-	0.969
TDDS			
any AS	0.768	0.729	0.905
significant AS	0.914	0.714	0.949
severe AS	0.965	-	0.980

Reference

1. Jeon J, Ha S, Yoon Y, et al. Echocardiographic view classification with integrated out-of-distribution detection for enhanced automatic echocardiographic analysis. *arXiv [eess.SP; 2023]. Available from: https://arxiv.org/abs/2308.16483.*

2. Tran D, Wang H, Torresani L, Ray J, LeCun Y, Paluri M. A Closer Look at Spatiotemporal Convolutions for Action Recognition. In: *Proceedings of the IEEE conference on Computer Vision and Pattern Recognition*. 2018:6450-6459.

3. Holste G, Oikonomou EK, Mortazavi BJ, Coppi A, Faridi KF, Miller EJ, et al. Severe aortic stenosis detection by deep learning applied to echocardiography. Eur Heart J. 2023;44:4592–4604.

4. Yu C, Gao C, Wang J, Yu G, Shen C, Sang N. BiSeNet V2: Bilateral Network with Guided Aggregation for Real-Time Semantic Segmentation. *International Journal of Computer Vision*. 2021;129:3051-3068.

5. Park J, Jeon J, Yoon YE, et al. Artificial intelligence-enhanced automation of left ventricular diastolic assessment: a pilot study for feasibility, diagnostic validation, and outcome prediction. *Cardiovasc Diagn Ther*. 2024;14:352-366.

6. Jeon J, Kim J, Jang Y, et al. A Unified Approach for Comprehensive Analysis of Various Spectral and Tissue Doppler Echocardiography. *arXiv [eess.IV; 2023]. Available from: https://arxiv.org/abs/2311.08439.*

7. Otto CM, Nishimura RA, Bonow RO, Carabello BA, Erwin JP 3rd, Gentile F, et al. 2020 ACC/AHA Guideline for the Management of Patients With Valvular Heart Disease: A Report of the American College of Cardiology/American Heart Association Joint Committee on Clinical Practice Guidelines. J Am Coll Cardiol. 2021;77:e25–e197.

8. Baumgartner H, Hung J, Bermejo J, Chambers JB, Edvardsen T, Goldstein S, et al. Recommendations on the Echocardiographic Assessment of Aortic Valve Stenosis: A Focused

Update from the European Association of Cardiovascular Imaging and the American Society of Echocardiography. *J Am Soc Echocardiogr*. 2017;30:372–392.

9. Xie E, Wang W, Yu Z, Anandkumar A, Alvarez JM, Luo P. SegFormer: Simple and efficient design for semantic segmentation with transformers. *Advances in neural information processing systems*. 2021;34:12077-12090.

10. Cubuk ED, Zoph B, Shlens J, et al. Randaugment: Practical automated data augmentation with a reduced search space. In: *Proceedings of the IEEE/CVF conference on computer vision and pattern recognition workshops*. 2020:702-703.

11. Ostvik A, Salte IM, Smistad E, et al. Myocardial Function Imaging in Echocardiography Using Deep Learning. *IEEE Trans Med Imaging*. 2021;40:1340-1351.

12. Loshchilov I, Hutter F. SGDR: Stochastic Gradient Descent with Warm Restarts. *arXiv [cs.LG; 2016]. Available from: https://arxiv.org/abs/1608.03983.*

13. Wessler BS, Huang Z, Long GM Jr, Pacifici S, Prashar N, Karmiy S, et al. Automated Detection of Aortic Stenosis Using Machine Learning. J Am Soc Echocardiogr. 2023;36:411–420.